nature research

https://doi.org/10.1038/s41563-020-00807-1

Supplementary information

Observation of fluctuation-mediated picosecond nucleation of a topological phase

In the format provided by the authors and unedited

Supplementary Information for: Observation of fluctuation-mediated picosecond nucleation of a topological phase

Felix Büttner[*], Bastian Pfau[*†], Marie Böttcher, Michael Schneider, Giuseppe Mercurio, Christian M. Günther, Piet Hessing, Christopher Klose, Angela Wittmann, Kathinka Gerlinger, Lisa-Marie Kern, Christian Strüber, Clemens von Korff Schmising, Josefin Fuchs, Dieter Engel, Alexandra Churikova, Siying Huang, Daniel Suzuki, Ivan Lemesh, Mantao Huang, Lucas Caretta, David Weder, John H. Gaida, Marcel Möller, Tyler R. Harvey, Sergey Zayko, Kai Bagschik, Robert Carley, Laurent Mercadier, Justine Schlappa, Alexander Yaroslavtsev, Loïc Le Guyarder, Natalia Gerasimova, Andreas Scherz, Carsten Deiter, Rafael Gort, David Hickin, Jun Zhu, Monica Turcato, David Lomidze, Florian Erdinger, Andrea Castoldi, Stefano Maffessanti, Matteo Porro, Andrey Samartsev, Jairo Sinova, Claus Ropers, Johan H. Mentink, Bertrand Dupé, Geoffrey S. D. Beach, and Stefan Eisebitt

[*]These authors contributed equally to this work
[†]Bastian.Pfau@mbi-berlin.de

S.1 Locating the skyrmion state in the center of the hysteresis loop

Figure S1 shows the average magnetization of domain states and skyrmion states in Pt/CoFeB/ MgO as a function of applied field, along with a hysteresis loop measured by focused magneto-optical Kerr effect polarimetry on the same sample. The average out-of-plane magnetization of the images was determined from their average gray contrast. As suggested in Fig. 1a of the main text, the area-averaged out-of-plane magnetization m_z of the skyrmion state is located between the two major hysteresis loops of the material.

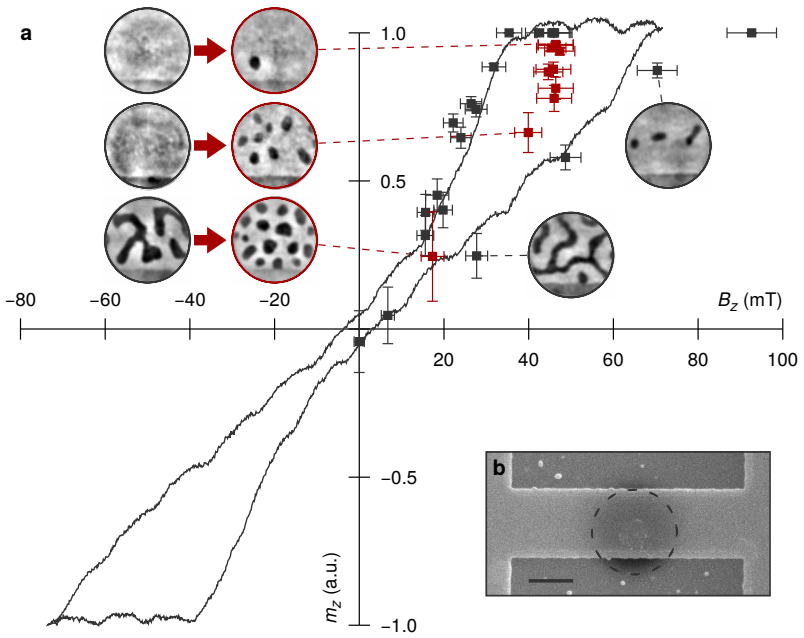

Figure S1. Field-dependent states in [Pt/CoFeB/MgO]$_{15}$ before and after laser-induced switching within the hysteresis loop of the magnetic track. (**a**) Magnetic hysteresis. The solid line represents the local Kerr signal. Single data points (shown in grey and red) are extracted from x-ray images, examples of which are shown as insets. Grey data points correspond to static field cycles before laser exposure. Red data points correspond to spin states reached by laser-induced topological switching. The net magnetization in the field of view reflects the average intensity of images after binarizing to values of $+1$ and -1 for up and down magnetization, respectively, based on the intensity histogram of the image. The error bars (std. dev.) derive from the spatial resolution of the x-ray images. The switching fluence was $\sim$16 mJ/cm^2. (**b**) SEM image of the magnetic stripline used for the experiment in (a). The dashed circle marks the field of view with a diameter of 1 µm. Scale bar, 500 nm.

S.2 Evolution of stripes to skyrmions by multiple shots

In Fig. S2 we show the images based on which Fig. 3a in the main text was constructed. One can see the gradual evolution of stripe domains to skyrmions with thousands of pulses for fluences <14.5 mJ/cm^2 while at larger fluences a single pulse is sufficient to produce a pure skyrmion state. Images at each fluence were recorded in sequence, starting from a saturated state (before the first pulse).

S.3 Switching threshold of Pt/Co

Figure S3 shows the density of skyrmions in Pt/Co as a function of laser fluence. As in Pt/CoFeB/MgO, we find a sharp fluence threshold above which the skyrmion density is approximately constant. The threshold value of 12 mJ/cm^2 is comparable to Pt/CoFeB/MgO. Note that for the lowest fluence used in the experiment, we observed no skyrmion nucleation in seven measurements.

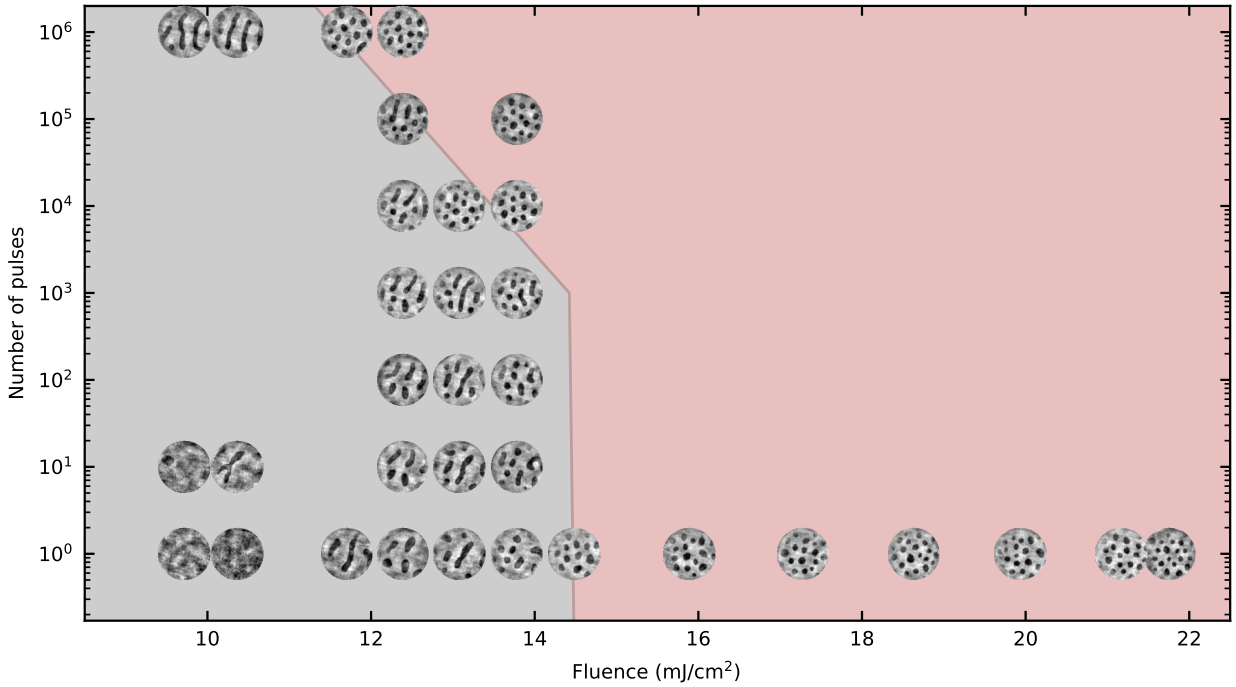

Figure S2. Magnetic textures as a function of pulse fluence and number of shots. Images correspond to the data points shown in Fig. 3a in the main text. The colored regions indicate which states we identify as skyrmions (blue) or mixed / saturated (orange). As pure skyrmion states we identify patterns of fully enclosed domains with a density that remains constant upon subsequent laser exposure. Note that equivalently, one can define those patterns as skyrmion states in which all domains are substantially circular. The equivalence is evident if one considers that any elongated domain occupies more space than a circular domain, thereby reducing the density of domains.

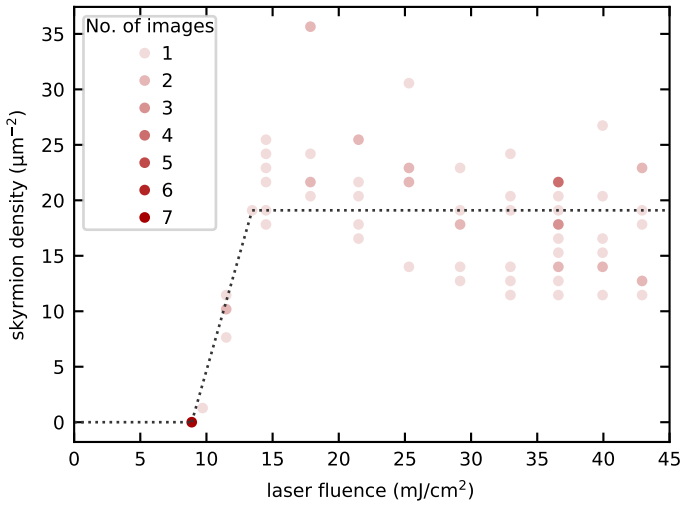

Figure S3. Fluence-dependent skyrmion density in Pt/Co. Density of skyrmions nucleated by single laser pulses from a saturated state in Pt/Co at a bias field of $B_z = 59\,\mathrm{mT}$. Each analyzed image is represented by a semi-transparent point in the graph. Darker points thus correspond to multiple measurements of the same result, as indicated in the legend. The line is a guide to the eye. The pure skyrmion phase is characterized by the upper plateau of the skyrmion density.

S.4 Quantitative analysis of the nucleation probability distribution

A quantitative measure of the degree of homogeneity of the probability distribution underlying an experimentally observed skyrmion distribution map is the variance of that distribution (i.e., of the number of skyrmions in each pixel) divided by the mean value of the distribution. As shown in Extended Data Figure 5, we expect that the variance-over-mean is ~ 1 for a homogeneous probability map, at least for the skyrmion sizes observed in the experiment and for a total skyrmion count ≤ 1000 (for much larger numbers, the variance-over-mean starts to differ from the shot-noise expectation of 1 because one skyrmion is larger than one pixel). By contrast, for a non-homogeneous distribution, we expect the variance-over-mean to be significantly larger than 1 (Extended Data Figure 5b shows the extreme case of a nucleation probability concentrated to just one nucleation site, i.e., one pixel). The experimental results are shown in Extended Data Figures 5c,d and can clearly be assigned to a predominantly homogeneous nucleation probability map (optically induced nucleation, Extended Data Figure 5c) and to an inhomogeneous nucleation map (nucleation induced by spin–orbit torques (SOT), Extended Data Figure 5d), respectively. The SOT data is from the experiment reported in Ref. [1], details about which can be found in that reference.

S.5 Fluence threshold for x-ray induced skyrmion nucleation

X-ray free-electron laser sources have a very high x-ray pulse intensity that can be sufficient to even evaporate or ablate the sample with a single shot. During our experiment we have used x-ray pulses of $\sim$6 mJ pulse energy. These pulses were subsequently attenuated by the monochromator (5×10^{-4} transmission), the refocusing optics ($\sim$90 % transmission) and the polarizer ($\sim$20 % transmission). Hence, in this configuration, the expected maximum energy per pulse at the sample was $\sim$55 nJ or, given a Gaussian x-ray spot size of 30 µm (full width at half maximum, FWHM), a fluence of 5.5 mJ/cm^2 in the centre of the spot. This is on the same order of magnitude as the threshold to nucleate skyrmions with infrared light. For pump-probe experiments, we needed to make sure that only the pump beam (the infrared beam) was nucleating skyrmions. We therefore further attenuated the x-ray beam by a variable pressure gas attenuator. To determine the nucleation threshold, we recorded small-angle x-ray scattering during a magnetic field cycle with various attenuation levels of the x-ray beam. The result is shown in Extended Data Figure 6, where each data point corresponds to an average over six x-ray shots per cycle and up to four full field cycles. A non-zero scattering intensity signifies the presence of non-uniform spin structures, such as domains and skyrmions [2]. Hence, from this data, we can extract the nucleation field H_n and the saturation field H_s, see Extended Data Figure 6. The corresponding fluences were measured on a per-pulse basis by a gas monitor detector (GMD) detecting photo-electrons and -ions. The pulse-resolved photo-electron signal was scaled to match the slower, but absolutely calibrated photo-ion signal [3]. This measurement does not include the transmission of the polarizer and refocusing optics, which are taken into account via their known transmission. The uncertainty of the final fluence value is given by the accuracy with which the x-ray spot size is known. To measure the spot size, we used a long-range microscope to observe

the x-ray induced fluorescence on a YAG screen in the sample plane, resulting in an uncertainty of $\sim$5 µm.

For a maximum x-ray fluence of (4.1 ± 1.2) mJ/cm^2 or higher (10 % gas attenuator transmission), we observe that, compared to lower x-ray intensities, H_n becomes larger (domains nucleate earlier when coming from saturation) and H_s becomes smaller (i.e., the last domains annihilate easier). This is consistent with the narrowing of the hysteresis loop after laser exposure shown in Fig. S1. We therefore conclude that above this threshold we see x-ray induced nucleation and annihilation of skyrmions or reversed domains. At (3.8 ± 1.1) mJ/cm^2 (7.5 % transmission) and below, both H_n and H_s are no longer x-ray fluence dependent. We therefore choose to operate at 7.5 % transmission. Note that, due to the large shot-to-shot intensity fluctuations, exceptionally high intensity pulses may still be above the nucleation threshold even at 7.5 % transmission. However, during the pump-probe experiments, we have stored the camera data of each shot separately and unusually intense x-ray pulses were not considered in the analysis (see Section S.7).

Note that the threshold fluences for x-ray induced switching are very similar to the infrared regime, supporting our interpretation that fast heating is driving the transition without particular sensitivity to the means by which the heating is achieved. However, considering the enormous pulse-to-pulse variation, our estimates of the x-ray fluences based on the optical density of the gas attenuator is highly approximate. Moreover, whether the x-ray nucleated spin textures are actually topological remains to be confirmed. While not being fully conclusive, our observations point to the possibility of x-ray pump – x-ray probe experiments, where larger penetration depth, element-selective excitations, and a potentially much smaller focus are only some of the prospective benefits compared to laser-driven excitations.

S.6 Masking of the time-resolved scattering camera images

We have used a DSSC detector [4, 5] comprising 16 rectangular pixel array modules arranged in a square grid. Each quadrant of this grid was covered by an Al filter to block the infrared beam. Moreover, there was a finite spacing between these modules. After mapping the data to this geometry, a camera image as shown in Fig. S4a is obtained (which shows an image without any x-ray scattering). Note that small uncertainties in the panel geometry arise from the fact that the detector is assembled from separate modules. While such uncertainties would impose a problem for imaging, they are irrelevant for our scattering analysis.

We have applied a mask to all recorded images to remove artifacts. First, we notice that there is still signal from the infrared beam very close to the centre of the detector. These regions were masked and removed. In addition, we have masked all pixels below the frame of the Al filter since these pixels did not detect any x-rays and only contributed to the noise. Finally, we have masked dead pixels. The result is shown in Fig. S4b. The same mask was applied to all frames. Note that masked pixels were ignored when normalizing the azimuthal integral of the scattered intensity.

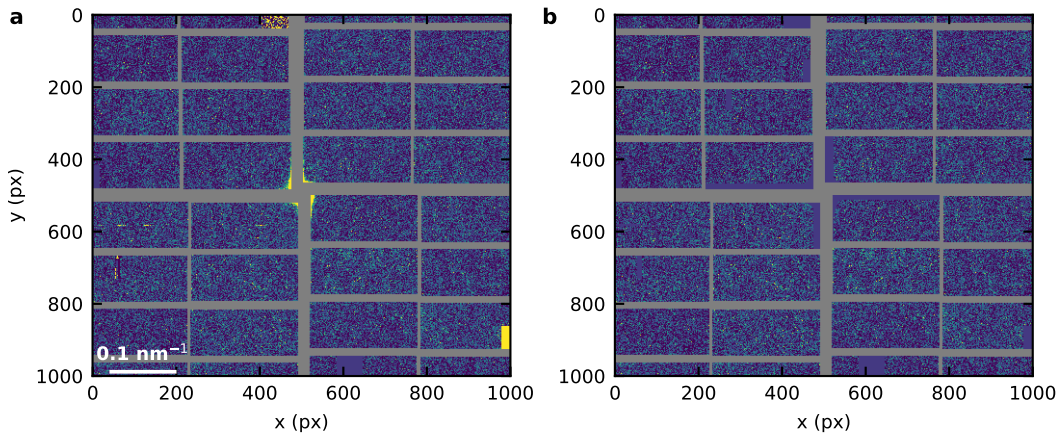

Figure S4. Masking of DSSC camera images for time-resolved x-ray scattering. (**a**) Cropped raw camera image after arranging the pixels according to the physical detector geometry and subtracting a dark frame. The image was recorded while exposing the sample with infrared light but not with x-rays. (**b**) Same image as in (a) after applying the mask filter. Note that images appear stretched along the x direction due to an hexagonal arrangement of the pixels, which leads to a pixel periodicity of 236 µm and 204 µm in x and y direction, respectively. This distortion was considered in our analysis.

S.7 Frame selection of time-resolved scattering data

The desired sequence of our time-resolved scattering experiments is illustrated in Extended Data Figure 7. In this scheme, a sequence starts by saturating the sample, followed by the reduction of the field and the exposure of the sample with a train of three x-ray pulses and one infrared laser pulse just before the second x-ray pulse. The field cycle ensures that the sample is prepared every time in a metastable uniform state where skyrmion nucleation is possible by ultrafast heating. However, our experiments were conducted during the early user startup phase of the European XFEL that normally delivers x-ray pulse trains at 10 Hz repetition frequency. This was too fast to cycle the magnetic field and on-demand request of x-ray pulses and magnetic fields was not fully implemented. We therefore have applied filters to select only those trains that actually represent the desired experimental sequence. Specifically, we considered only trains where all of the following conditions were fulfilled:

1. The train includes exactly three x-ray pulses.
2. The previous train does not include any x-ray pulses.
3. All x-ray pulses in the train were of significant intensity to give a statistically meaningful scattering pattern (see Fig. S5).
4. The intensity of the first x-ray pulse in the train was below a threshold to exclude skyrmion nucleation by the x-ray pulse (see Fig. S5).
5. The initial state is magnetically uniform (integrated scattering intensity below threshold, see Fig. S6). This criterion makes sure that the state was properly reset by the magnetic field.

6. The final state is a skyrmion state (integrated scattering intensity above threshold, see Fig. S6). This selection is required because the magnetic field for some pump-probe trains was still high, preventing skyrmion formation.

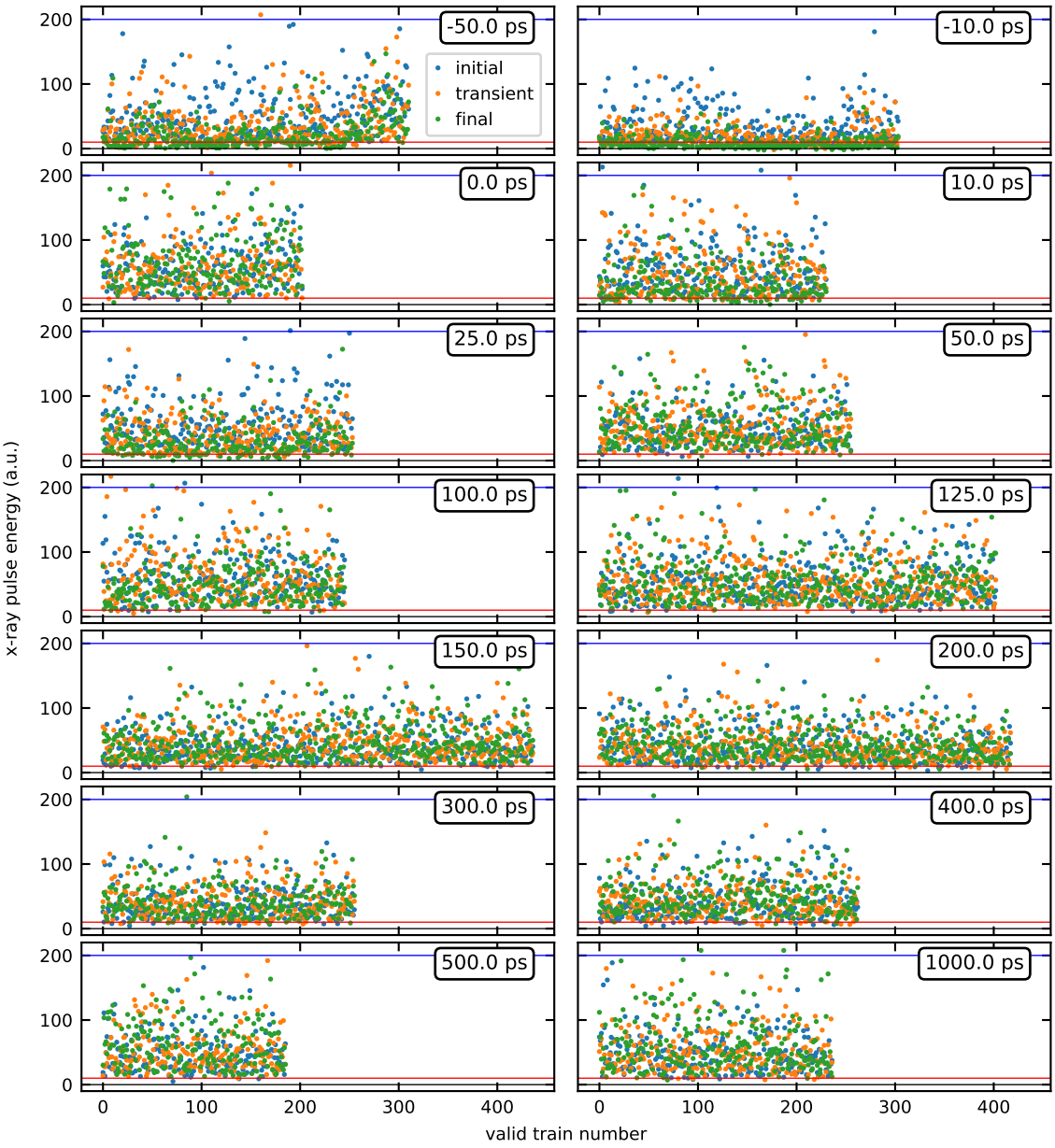

Figure S5. Threshold selection of trains by x-ray pulse intensity. Each panel shows the x-ray pulse intensity as measured with a gas intensity monitor after the monochromator in the beamline. We select only trains where the intensity of all three x-ray pulses is above the detection limit (red line) and where the intensity of the first x-ray pulse is below the empirical x-ray skyrmion nucleation threshold (blue line; see also Extended Data Figure 6).

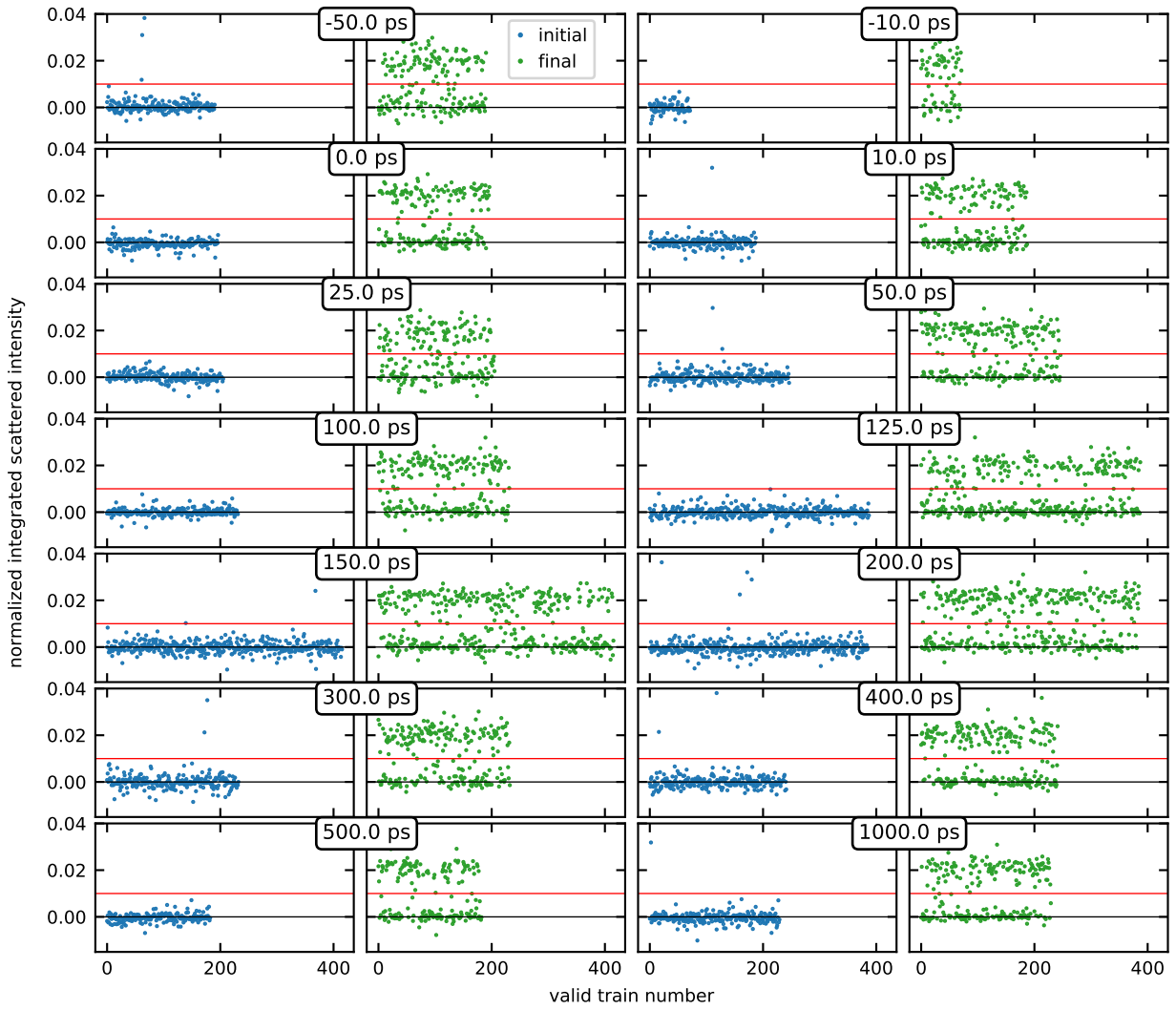

Figure S6. Threshold selection of trains by normalized scattered intensity in the initial and final state. For each time delay we plot the normalized integrated scattered intensity of all pulse trains that have passed tests 1-4. We notice a binary distribution in the final state intensity, which represents the case of skyrmion nucleation (high value) and no skyrmion nucleation (low value). We select only those trains where the final state scattered intensity is high, i.e., where skyrmions were nucleated. Below-threshold data represents trains recorded at a high magnetic field where skyrmion nucleation was not possible. In addition, we discard the few trains where the initial state intensity is above the threshold, i.e., where the skyrmion state was not successfully reset by the magnetic field.

S.8 Control measurement: constant initial and final state scattering

Each pump-probe measurement was accompanied by a control measurement of the initial state (60 µs before the laser pulse) and the final state (60 µs after the laser pulse). The $I(q,t)$ intensity maps of these control data are shown in Figs. S7 and S8 (where t is the time delay of the corresponding pump-probe data). The experiment was conducted in descending sequence starting from large time delays (with the exception of $t = 0\,\mathrm{ps}$, which was recorded first). The initial state data reveals a slowly increasing background count towards later measurement times (earlier pump-probe delays). This background was subtracted from the transient and final state data. After background correction, the final state scattering is almost perfectly constant as a function of t, confirming that the transient state time-dependent data is in fact only related to transient changes of the magnetic pattern.

S.9 Robustness of the fit of the total integrated intensity

The total integrated intensity in Fig. 4d in the main text was obtained by summing the intensities of all pixels up to a cutoff q_{max} value. The reason for the cutoff is that very high q pixels contribute more noise than data, making the extracted total intensity less meaningful. To confirm that the physical interpretation does not depend on our choice of the integration cutoff, we plot in Fig. S9 the fit parameters for a broad range of cutoff values. While the inflection point of $I(t)$ shows considerable variation, both the timescale of equilibration and the saturation at 300 ps are robust with respect to the integration cutoff.

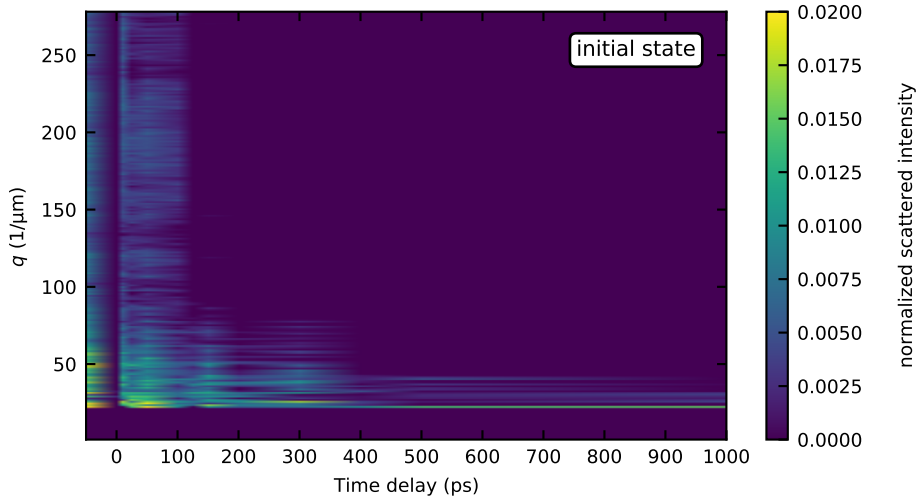

Figure S7. Initial state q-dependent scattering as a function of delay of the transient state x-ray pulse. The small signal at small time delays is due to thermal drift of the readout noise. This offset was subtracted from the transient and final state data.

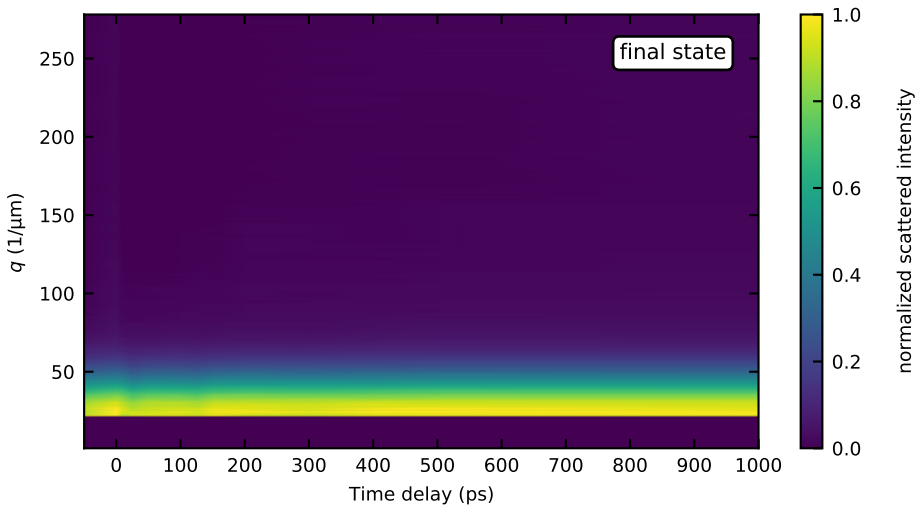

Figure S8. Final state q-dependent scattering as a function of delay of the transient state x-ray pulse. The signal is flat, indicating stable pump-probe conditions during our experiment.

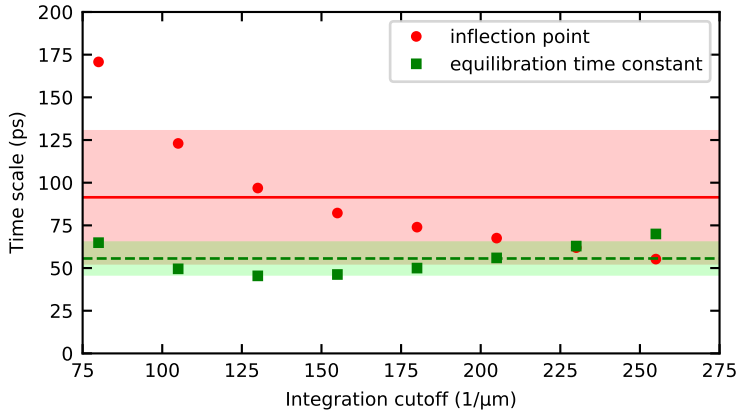

Figure S9. Total intensity fit results as a function of integration cutoff. Data points show the inflection point (time delay where the change of total intensity is largest) and the exponential equilibration time constant extracted from a logistic function fit to the integrated intensity for variable cutoff value of the integration. The dashed lines represent the averages and the bands indicate the one standard deviation error bar on each side of the average.

S.10 Analysis of scattering spectra

In Extended Data Figure 8 we show the complete set of scattering spectra, where all previously discussed corrections have been applied. The transient data (orange) is initially almost constant as a function of q, i.e., there is significant intensity scattered to high angles. At later times, transient spectra exhibit a pronounced intensity maximum at low momentum transfer. For comparison, we also show the spectra of the initial (blue) and final state (green). We do not detect any scattering in the initial state and all final state spectra are identical within the experimental shot noise (see also Figs. S7 and S8). At 1 ns of time delay between pump and probe the scattering function of the transient state is already similar to the one of the final state, even though it has not yet reached the full intensity.

Our scattering data can be seen as a superposition of two main contributions: scattering off a single skyrmion nucleus (the so-called form factor), which is characteristic of its size and shape, and scattering off the ensemble of skyrmions (the structure function), which encodes the positions of skyrmions relative to each other. Given the high density of skyrmions, both the size and the relative distance are of similar order of magnitude and the scattering signals strongly overlap. Lacking a reliable quantitative model of the transient spin textures in our experiment, those contributions cannot be disentangled analytically. Instead, we obtain approximate estimates of the mean skyrmion distance and size from the most distinctive features of our recorded intensity spectra, namely the position of the intensity maximum q_{peak} and a section of the high-q shoulder of this maximum where $\ln(I(q))$ decreases linearly with q^2, respectively. These features can be identified starting with a delay of 100 ps after the pulse.

The intensity maximum reflects the correlation in the positions of the skyrmions and, thus, acts as a measure for the mean distance between the skyrmions. We therefore calculate the average skyrmion distance via $2\pi/q_{\text{peak}}$. To determine q_{peak}, we fit the $I(q)$ spectra near the peak with a parabola $I(q) = a(q - q_{\text{peak}})^2 + c$, see Extended Data Figure 9. Note that the same results were obtained when fitting with a Voigt function. The temporal evolution of the fit parameters is shown in Fig. S10.

A size estimate of the skyrmion nuclei is extracted from a Guinier fit. The Guinier approximation predicts for the scattering of dilute particles for small q (typically $r_G q < 1$):

$$\ln(I(q)) - \ln(I(0)) \simeq -\frac{1}{3} r_G^2 q^2 \,. \tag{1}$$

Here, r_G is called the "radius of gyration" of the scattering particle.

In Extended Data Figure 10 we show $\ln(I)$ vs. q^2 plots of the SAXS spectra. At the high-q side of the intensity maximum, we find a regime in which this graph is linear, i.e., where $\ln(I(q))$ is directly proportional to q^2. To obtain r_G, we perform a linear regression in this region. Following the recommendations in [6], we iteratively refine the fit range and use an upper limit of $r_G q \leq 2.0$ where the Guinier fit is still meaningful with acceptable error. For our data, the lower limit for the fit is given by the scattering intensity maximum due to the inter-particle correlation. We, thus, define the fit range to $1.5 \leq r_G q \leq 2.0$, consistently for all delay times.

The radius of gyration is a direct measure of the size of the scattering particles (i.e., the skyrmions)

which we assess by their mean diameter as $d \simeq 2\chi r_G$ [6]. The proportionality factor χ depends on many parameters, such as the shape, size distribution and spatial distribution of the particles as well as the fit range (a fit at larger $r_G q$ results in larger error of χ). The most accurate estimate of χ is obtained in the final state, where direct real-space information is available. A histogram of the skyrmion size distribution is presented in Fig. S11 revealing a mean skyrmion diameter of 73 nm, corresponding to $\chi = 0.83$. With a known value of χ, our method is very precise, as evidenced by the very small variation of the final state mean diameters shown in Fig. 4d of the main paper. To account for the fact that shape and distribution of the skyrmions in the intermediate state likely deviate from the final state properties in an unknown way, we use the same χ for the intermediate state conversion but add a systematic error of 30 %, which is on the high side of expected uncertainties corresponding to our fit range [6].

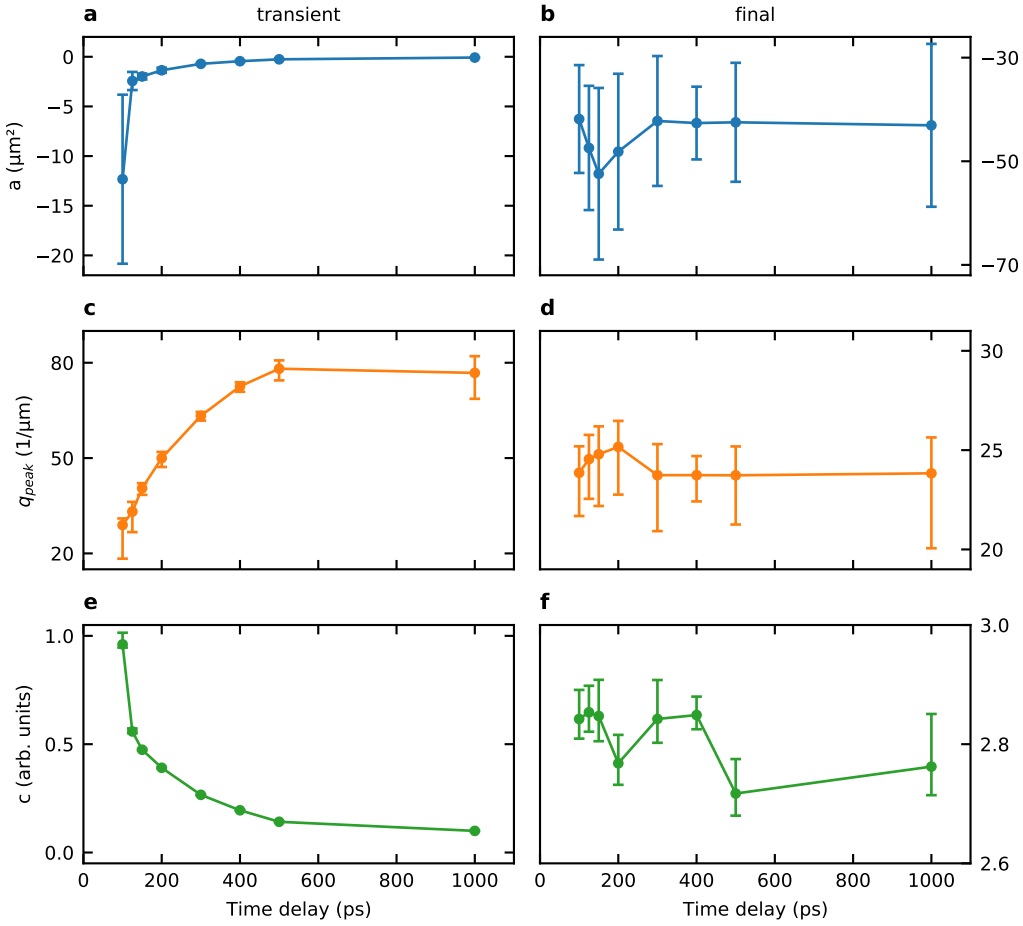

Figure S10. Fit parameters of the peak fit as a function of pump-probe delay.

S.11 Supplementary Video

The video shows four panels. On top is a plot of the total topological charge and the bath temperature as a function of time. A black vertical line indicates the current time of the simulation. Below are three panels, showing the normalized out-of-plane magnetization, the local topological charge density, and

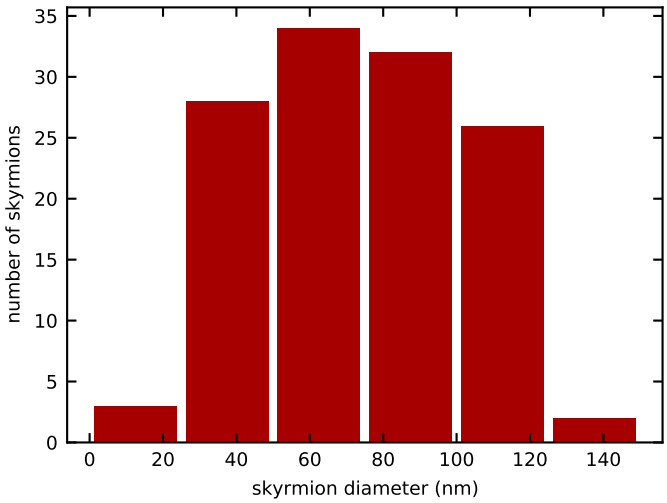

Figure S11. Histogram of the skyrmion size distribution in Pt/Co in the final state The histogram was compiled from six holography images recorded using the same conditions as in Fig. 2c, top row, of the main paper.

a low-pass filtered version of the local topological charge density, where the filter size of the low-pass filter in reciprocal unit cells is indicated in the filtered image.

References

[1] Büttner, F. *et al.* Field-free deterministic ultrafast creation of magnetic skyrmions by spin–orbit torques. *Nature Nanotechnology* **12**, 1040–1044 (2017).

[2] Hellwig, O., Maat, S., Kortright, J. B. & Fullerton, E. E. Magnetic reversal of perpendicularly-biased Co/Pt multilayers. *Physical Review B* **65**, 144418 (2002).

[3] Grünert, J. *et al.* X-ray photon diagnostics at the European XFEL. *Journal of Synchrotron Radiation* **26**, 1422–1431 (2019).

[4] Porro, M. *et al.* Development of the DEPFET Sensor With Signal Compression: A Large Format X-Ray Imager With Mega-Frame Readout Capability for the European XFEL. *IEEE Transactions on Nuclear Science* **59**, 3339–3351 (2012).

[5] Hansen, K. *et al.* Qualification and Integration Aspects of the DSSC Mega-Pixel X-Ray Imager. *IEEE Transactions on Nuclear Science* (2019).

[6] Feigin, L. A. & Svergun, D. I. *Structure Analysis by Small-Angle X-Ray and Neutron Scattering* (Plenum Press, New York, NY, USA, 1987).